ChemPubSoc Europe

DOI: 10.1002/cssc.201501621

CHEMSUSCHEM Full Papers

Biomass-Derived Electrode for Next Generation Lithium-Ion Capacitors

Palanichamy Sennu,[a] Vanchiappan Aravindan,[b] Mahadevan Ganesan,[c] Young-Gi Lee,[d] and Yun-Sung Lee*[a]

We report the fabrication of a carbon-based high energy density Li-ion hybrid electrochemical capacitor (Li-HEC) from low cost and eco-friendly materials. High surface area ($2448 \pm 20\ m^2 g^{-1}$) activated carbon (AC) is derived from the environmentally threatening plant, *Prosopis juliflora*, and used as the positive electrode in a Li-HEC assembly. Natural graphite is employed as negative electrode and electrochemically pre-lithiated prior to the Li-HEC fabrication. The Li-HEC delivers a specific energy of $162.3\ Wh\,kg^{-1}$ and exhibits excellent cyclability (i.e., ~79% of initial capacity is retained after 7000 cycles). The superior electrochemical performance of Li-HEC benefits from the tube-like unique structural features of the AC. Also, the presence of a graphitic nanocarbon network improves the ion transport, and the formed micro- and meso-porous network acts as reservoir for the accommodation of charge carriers.

Introduction

Environmentally begin utilization of natural energies, such as solar, wind power, and geo-thermal energy, for portable electronic devices and electrical vehicles is a key revolution in energy storage device development. The worldwide increasing production and adoption cost for hybrid electrical vehicles (HEV) will reach 40 billion USD by 2020, and their power capability is also limited to approximately 250–340 $W\,kg^{-1}$.[1,2] In recent years, advanced hybrid devices are the most promising storage systems for large scale smart-grid and industry applications. Compared to secondary batteries, Li-ion hybrid electrochemical capacitors (Li-HEC) possess high energy density, high power capability, and long-term stability.[3] Generally, Li-HECs are constructed with electrical double layer (EDL) materials as the positive electrode (supercapacitor component) and Li-intercalation-type materials as the negative electrode (Li-ion battery component).[4–6] The emergence of innovative electrode materials clearly provided opportunities in the field of electrochemical energy storage and direct correlations with availability, cost, and safety are considered. Recently, numerous insertion electrodes like $Li_4Ti_5O_{12}$,[7] hard carbon, graphite, TiO_2-B,[8] LiCrTiO_4,[9] $TiNb_2O_7$,[10] $LiTi_2(PO_4)_3$,[11] β-FeOOH,[12] and a variety of high surface area carbonaceous materials, such as activated carbons (AC), templated porous carbon,[13] carbon aerogel, and graphene, in both native and activated form,[14–19] were exploited for Li-HEC applications. Owing to the higher redox potential of the metal oxides, the energy densities of the Li-HECs are restricted to below 90 $Wh\,kg^{-1}$, which is insufficient for the practical use.[20–22] Therefore, utilization of either pre-lithiated graphite or pre-lithiated hard carbon is the only available option to explore as the insertion-type electrode to achieve an energy density of beyond 150 $Wh\,kg^{-1}$. On the other hand, a counter electrode with high surface area AC and tailored micro-/meso-porosity is required to fulfil the goal.[23] AC derived from agricultural by-products is highly attractive because of the recycling.[23] Further, natural abundance and structural doping of different electron-donating heteroatoms (e.g., N, S, B) from cellulose are worth mentioning for such biomass products.[23] Further, to date, most of the studies on Li-HEC are targeted on the development of higher performance Li-insertion-type electrodes, as discussed above, with commercially available AC as the counter electrode. Although, biomass-derived AC was widely explored as a potential electrode for the fabrication of high performance supercapacitors, but studies were limited to aqueous and organic configurations.[24–26] Herein, we extended the possibility of using such biomass-derived carbonaceous materials with active functional groups in a Li-HEC configuration to widen the energy density. After considering many options, we chose environmentally threatening *Prosopis juliflora* (PJ) as a precursor to yield a high surface area AC (PJ-

[a] *P. Sennu, Prof. Y.-S. Lee*
Faculty of Applied Chemical Engineering
Chonnam National University
Gwang-ju 500-757 (Republic of Korea)
E-mail: leeys@chonnam.ac.kr

[b] *Dr. V. Aravindan*
Energy Research Institute @ NTU (ERI@N)
Nanyang Technological University, Research Techno Plaza
50 Nanyang Drive
Singapore 637553 (Singapore)

[c] *Dr. M. Ganesan*
Electrochemical Power Sources Division
CSIR-Central Electrochemical Research Institute
Karaikudi 630006 (India)

[d] *Dr. Y.-G. Lee*
Power Control Device Research Team
Electronics and Telecommunications Research Institute
Daejeon 305-700 (Korea)

Supporting Information and the ORCID identification number(s) for the author(s) of this article can be found under http://dx.doi.org/10.1002/cssc.201501621.

AC). Generally, the PJ plant absorbs water from both the soil and atmosphere and emits CO_2. PJ is an invasive weed and predominantly grows in Africa, Asia, Australia, and North/South America. Conversion of PJ into a useful material leads to protection of the soil and provides a high performance material for energy storage applications in a cost effective manner.[27,28] Accordingly, a Li-HEC was fabricated using electrochemically pre-lithiated natural graphite (NG) and PJ-AC as negative and positive electrodes, respectively. Prior to the Li-HEC assembly, both the AC and graphite electrodes were tested with Li in a half-cell configuration to determine the charge balance between positive and negative electrodes. Also, the synthesized PJ-AC and NG are systematically characterized with various characterization techniques and described in detail.

Results and Discussion

The XRD pattern of PJ-AC and NG are shown in Figure 1a. The PJ-AC pattern shows two broad diffraction peaks at 25 and 43° with low intensity that are indicative of amorphous natured semi-graphitic carbons. On the other hand, the XRD pattern of NG showed the characteristic reflections that are consistent with NG. Figure 1b shows the Raman spectra of PJ-AC and NG. Two intense reflections observed at ~1584 and ~2688 cm^{-1} for PJ-AC are assigned to the G and 2D bands of carbon, respectively.[29,30] The observed reflections are characteristic for carbonaceous materials and can be used as the fingerprint for graphite, which is naturally present in PJ-AC. A broad band at around ~1348 cm^{-1} (D peak) corresponds to the disordered nature or imperfectness in the carbon structure. The intensity ratio between D and G bands (I_D/I_G) was calculated to be ~0.64, which clearly suggests that PJ-AC has a high degree of graphitization and ordered structure.[11,29] The most obvious differences in the 2D bands are the shape and position of NG 2D peak; they are shifted towards higher wavenumber (~2715 cm^{-1}) compared to PJ-AC (~2689 cm^{-1}). Further, the 2D band of PJ-AC is much more intense than in NG (Figure S1).

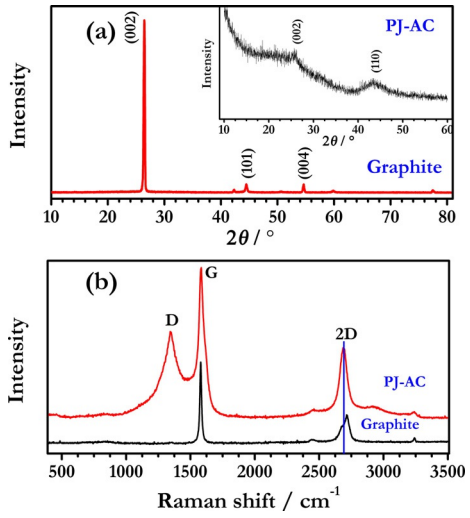

Figure 1. (a) XRD pattern of NG and PJ-AC (inset), and (b) Raman spectra of PJ-AC and NG.

The peak shift in NG is a result of interactions between the stacked graphene layers, which have a tendency to shift the bands to higher frequency, and it reveals a formation of few layer of graphene (between one and four layers) in PJ-AC at 900 °C.[31]

Surface area is one of the most important parameters for the accumulation of charge carriers on the surface towards double layer formation across the electrode–electrolyte interface. Thus, N_2 adsorption–desorption studies are conducted along with pore size distribution and presented in Figures 2

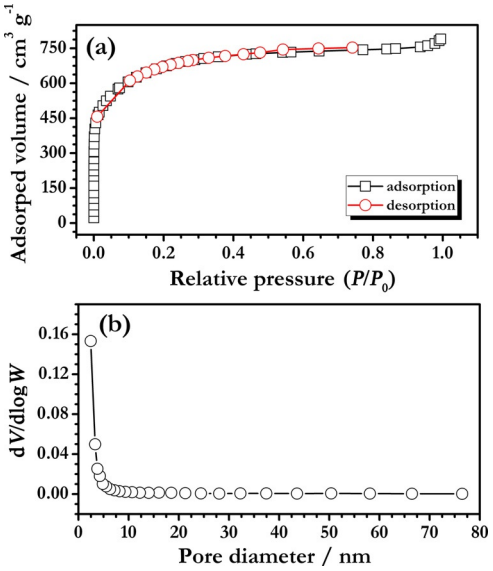

Figure 2. Brunauer–Emmett–Teller (BET) specific analysis, (a) N_2 adsorption–desorption isotherms, and (b) pore size distribution of PJ-AC.

and S2. According to the IUPAC classifications, the observed isotherm of PJ-AC is type-I. A sharp N_2 adsorption takes place at relatively low pressure ($P/P_0 < 0.2$) and slight adsorption takes place at high pressure ($P/P_0 > 0.9$), which implies that PJ-AC is composed of both micro- and meso-pores. The specific surface area and total pore volume of PJ-AC is calculated to be $2448 \pm 20\ m^2 g^{-1}$ and $1.212\ cm^3 g^{-1}$, respectively. The absence of a hysteresis loop between adsorption and desorption isotherms indicates that the pores are wedge or tubular shaped.[32] In contrary (Figure S2), the shape of isotherms clearly suggests the non-porous nature of the NG obtained from the commercially available sources. A comparison of the specific surface area, total pore volume, and meso- and micro-pore volumes of PJ-AC and NG are given in Table 1.

The morphological features of as prepared PJ-AC and NG are shown in Figure 3. From Figures 3a and S3, the SEM images of PJ-AC are naturally consisting of a tube-like structure. A thin layer of graphitic carbons are formed during the high temperature activation process. This is evident from the Raman analysis. Furthermore, the chemical activation process highlights the highly porous nature of the carbon with different size distribution. However, NG exhibits a flake-like morphology (Figure 3b). The elemental composition of PJ-AC was investigated by X-ray photoelectron spectroscopy (XPS) and

Table 1. BET surface area, total pore volume, and average pore diameter of PJ-AC and NG.

Sample	S_{BET} [a] [$m^2 g^{-1}$]	V_{total} [b] [$cm^3 g^{-1}$]	V_{micro} [c] [$cm^3 g^{-1}$]	V_{meso} [d] [$cm^3 g^{-1}$]	d_{avg} [e] [nm]
PJ-AC	2448	1.2116	1.1191	0.0925	1.9796
NG	3.6	0.04013	–	–	44.5

[a] S_{BET} is the BET surface area and it was measured at relative pressure of 0.990. [b] Total pore volume (V_{total}) was the single point adsorption total pore volume of pores less than 400 nm diameter at $P/P_0 = 0.990$. [c] V_{micro} is the micropore volume. [d] V_{meso} is the mesopore volume. [e] d_{avg} is the average pore diameter.

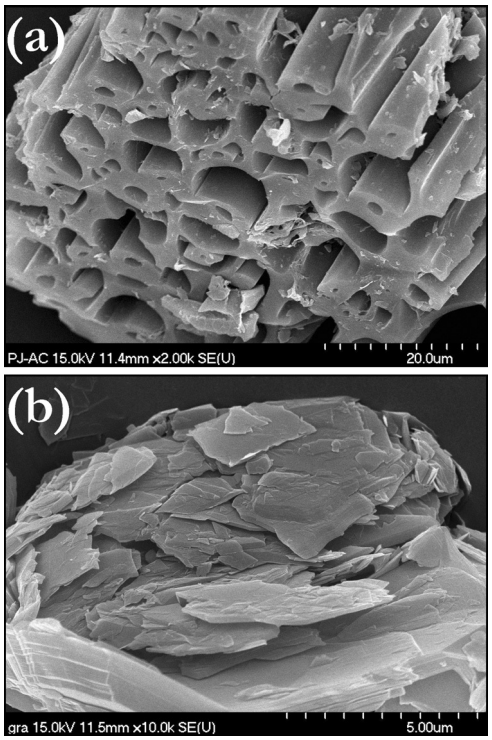

Figure 3. SEM images of (a) tube-like PJ-AC and (b) NG powder.

the core level analysis of different hetero-elements and weight percentage are given in Figure S4 and Table 2. The PJ-AC naturally contains various elements like C, O, Ca, S, and N which are clearly seen in survey spectrum. Specifically, the Ca 2p spectrum contains two main peaks located at ~347.82 eV for Ca $2p_{3/2}$ and ~351.45 eV for Ca $2p_{1/2}$. The spin-orbit splitting is ~3.63 eV, which confirmed that the Ca 2p existed as Ca–O or Ca–CO_x compositions.[33] The N 1s (1.11 wt%) and S 2p (0.81 wt%) peaks located at ~400.07 and ~168.8 eV originated from C–NH_2 and C–SO_x, respectively.[34,35] The high resolution core level spectrum of C 1s and O 1s are given with its functional group.[34,36–38]

Prior to the fabrication of Li-HEC, adjusting the charge balance between the electrodes was necessary to yield high energy density, as the cathode (PJ-AC) and anode (NG) materials involved different reaction mechanisms with Li. In this regard, half-cell studies were performed at constant current

Table 2. The weight percentage of different elements present in PJ-AC from XPS analysis.

Element	Weight [%]
C	77.63
O	16.95
Ca	3.5
N	1.11
S	0.81

rate (0.1 A g^{-1}) for both PJ-AC and NG and the data is presented in Figure 4. Figure 4a shows the 1st, 2nd, and 3rd galvanostatic charge–discharge curves of NG between 0.05–1.5 V versus Li. In the first cycle, NG displayed the discharge and charge capacities of ~414 and ~355 mAh g^{-1}, respectively. The initial columbic efficiency is found to be ~86% and, in subsequent cycles, beyond 99% was observed. The large irreversible capacity in the first cycle is mainly attributed to the decomposition of electrolyte solution and subsequent solid electrolyte interface formation (SEI) over NG.[39] On the other hand, PJ-AC displayed the characteristic linear charge–discharge curves of between 2–4 V versus Li and are shown in Figure 4b. This linear curve shows the reversible adsorption–desorption of both anion and cation over the surface of PJ-AC, which clearly shows the perfect non-Faradic capacitive reactions.[40] Generally, above and below 3 V versus Li suggests the electric double layer formation with PF_6^- and Li^+, respectively. The Li/PJ-AC cell displayed an initial discharge capacity of ~98 mAh g^{-1} and stabilized in further cycles.

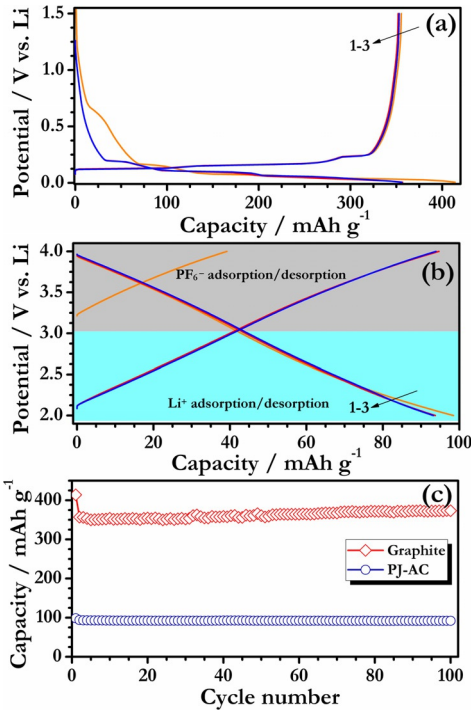

Figure 4. Galvanostatic charge–discharge profile for (a) NG and (b) PJ-AC in a single-electrode (half-cell) configuration between 0.05–1.5 and 2–4 V versus Li, respectively. (c) Cycling profiles of NG and PJ-AC at current rate of 0.1 A g^{-1}.

Cyclic performance of both NG and PJ-AC in half-cell assemblies is shown in Figure 4c. Very stable cycling profiles are realized for both materials (e.g., discharge capacities of 373 and 92 mAh g^{-1} are noted after 100 cycles for NG and PJ-AC, respectively). This excellent cycle stability of PJ-AC is attributed to the improved access of both anion and cation to the inner part of electrodes (i.e., tailored porosity upon cycling). To achieve charge balance between the electrodes in Li-HEC, based on the specific capacity of individual electrodes with metallic Li, the mass ratio of PJ-AC with respect to NG was balanced to be 3.6:1. The electrochemical performance of the Li-HEC at this optimal mass ratio was further investigated in the presence of same electrolyte solution.

After adjusting the mass loading, the NG is pre-lithiated (PrG) in half-cell assembly and paired with PJ-AC in the presence of 1 M $LiPF_6$ in EC:DMC. The electrochemical performance of Li-HEC is shown in Figure 5. Figure 5a and S5 shows cyclic voltammetry (CV) traces of Li-HEC measured at different scan rates (0.5–10 mV s^{-1}) between 2–4 V. The integration of the net area under the CV curves showed the linear variation with respect to scan rate. The curve shape is a typical rectangular at lower scan than those obtained at high scan rates, which indicates the Faradaic reaction is dominated at low scan rate and non-Faradaic reactions is a prevailing factor at high scan rate. The distorted narrower loop is observed at higher scan rates owing to the stimulating large ohmic resistance in electrodes. Also, the graphitic anode delivers inferior electrochemical activity at high current rates that cannot be ignored. The galvanostatic charge–discharge study of Li-HEC was performed at various current densities from 0.05 to 1.5 A g^{-1} (Figures 5b and S6). Here, the applied current densities are calculated based on the total mass of both electrodes. The observed discharge times are converted into specific capacities according to Equation (1).[41]

$$\text{Specific capacity} = \frac{i(\text{mA}) \times t(\text{sec})}{3600 \times m(\text{g})} \quad (1)$$

$$\text{PD} = \frac{i(\text{A}) \times \Delta V}{m(\text{mg}) \times 10^{-6}} \quad (2)$$

$$E = \frac{\text{PD} \times \Delta t}{3600} \quad (3)$$

Where, i is applied current (A), t is total discharge time (s), m is total weight of active materials in both electrodes (14.2 mg), PD is the power density, and ΔV is average working potential [(2+4)/2=3 V]. Accordingly, specific capacity of Li-HEC is calculated to be 108, 104, 97, 82, 66, and 50 mAh g^{-1} at a current density of 0.05, 0.1, 0.2, 0.5, 1, and 1.5 A g^{-1}, respectively. The symmetrical patterns of charge–discharge curves suggests that charges are stored in a capacitive way. Figure 5c presents the cycling performance of Li-HEC up to 7000 cycles recorded at a constant current density of 0.5 A g^{-1}. The Li-HEC rendered ~79% of initial capacity values after 7000 cycles with Coulombic efficiency of >99% for throughout the cycle. Though, the presence of trace amount of Ca is detected in PJ-AC, but there is no detrimental effect on the performance of Li-HEC noted upon long term cycling.

Figure 6 shows typical comparison Nyquist plots of Li-HEC reordered before and after 1000 cycles. The EIS curve exhibits a semicircle in the high frequency region followed by an inclined line in the low frequency region. After cycling, both solution resistance (R_S) (from 8.33 to 5.62 Ω) and charge transfer resistances (R_{CT}, from 14.098 to 10.083 Ω) are decreased. The decrease of R_{CT} is a result of activation of functional groups present in the PJ-AC that certainly improves the conductivity of the PJ-AC. Nevertheless, reduced surface resistivity and the cracked porous structure allow facile ions diffusion to the interior of PJ-AC which cannot be ruled out. This result clearly

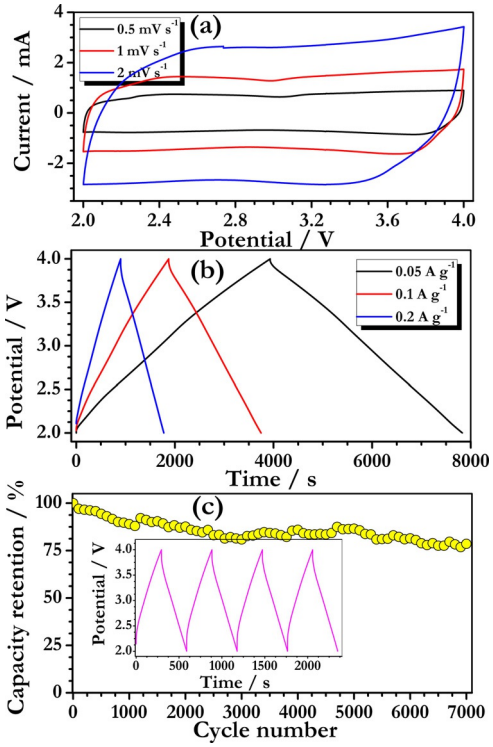

Figure 5. (a) CV traces of PJ-AC/PrG-based Li-HEC at various scan rates recorded between 2–4 V, (b) Galvanostatic charge—discharge profile of Li-HEC at various current densities, and (c) plot of cyclic retention versus cycle number of Li-HEC at a current density of 0.5 A g^{-1}. Inset: typical charge–discharge curves for the first 5 cycles.

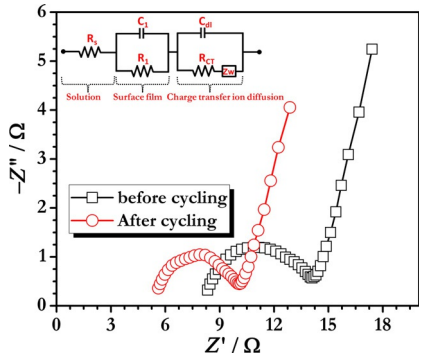

Figure 6. Comparison Nyquist plots of PJ-AC/PrG-based Li-HEC before and after 1000 cycles. Inset showed the corresponding equivalent circuit.

demonstrated an outstanding synergistic performance both electrodes, which translates into superior electrochemical performance of Li-HEC.

The Ragone plot of Li-HEC is shown in Figure 7. The energy density can approach 162.3 Wh kg^{-1} at a power of 150 W kg^{-1}

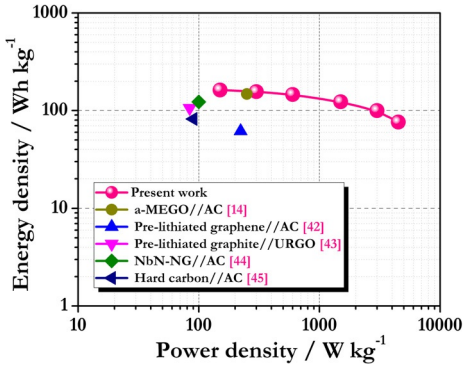

Figure 7. Ragone plot of PJ-AC/PrG-based Li-HEC.

are among the best reported values for carbon based Li-HEC to date. The power (PD) and energy density are calculated from Equations (2) and (3). Even after increase in the power to 4500 W kg^{-1}, the energy density still remained as ~76.3 Wh kg^{-1}, which is much higher than AC/$Li_4Ti_5O_{12}$-based systems. Also, this high energy density offset the other carbon-based Li-HEC reported elsewhere [e.g., activated microwave expanded graphite oxide (a-MEGO)//graphite in Li-electrolyte (147.8 Wh kg^{-1}),[14] pre-lithiated graphene//AC (61.7 Wh kg^{-1}),[42] pre-lithiated graphite//urea reduced graphitic oxide (URGO, 106 Wh kg^{-1}),[43] Li decorated niobium nitride/nitrogen-doped graphene hybrid material (NbN/NG)//AC (122.7 Wh kg^{-1}),[44] and hard carbon with stabilized Li metal powder//AC (82 Wh kg^{-1})].[45] We strongly believe the superior electrochemical performance of Li-HEC are mainly ascribed to the (i) tube-like cracked structured AC, which allows easier transportation of the charge carriers and can easily access the complete active material, (ii) the large specific surface area with tailored porosity certainly accommodates more Li^+ and PF_6^-, which can easily adsorbed/desorbed on surface of PJ-AC, (iii) a relative percentage of N and S and its synergistic effect in PJ-AC providing more Li-ion binding sites,[46] which obviously enhances the specific energy and powder capability of Li-HEC, (iv) presence of layered type of thin graphitic layers on PJ-AC facilitates fast electron transport to realize the high performance Li-HEC, and (v) the source material for the AC cannot be ruled out. Further studies are in progress on the counter electrode, especially the insertion-type material (e.g., hard carbon), to widen the energy density of the Li-HEC.

Conclusions

We successfully fabricated the carbon-based Li-ion hybrid electrochemical capacitors (Li-HEC) from eco-friendly and low cost carbon materials as the high surface area supercapacitor component. The activated carbon (AC) was derived from the environmentally threatening bio-source *Prosopis juliflora* (PJ) with tailored micro-/meso-porosity and high surface area. Li-HEC was fabricated with the pre-lithiated natural graphite (PrG) as counter electrode and delivered a maximum energy density of ~162.3 Wh kg^{-1} with excellent cyclability. The excellent stability and performance is not only ascribed to the synergistic effect of heteroatoms like (N, S, and Ca) present in the PJ-AC, also with tube like morphology with mesoporous structure, and existence of O functional groups. The conversion of an environmentally threatening plant in to a high performance electrode certainly provides the new avenues to eradicate such plant from the soil in a useful manner.

Experimental Section

Preparation of PJ-AC

PJ wood/stem was used as the starting material. First, PJ wood was cut in to small pieces and charred. Then, the charred PJ was ground into a fine powder and treated with 1:2 weight ratio of KOH at 120 °C for 3 h. Then, the mixture was activated at 900 °C under an N_2 flow at a heating rate of 5 °C min^{-1} for 3 h. After cooling to room temperature, the resultant product was washed thoroughly with de-ionized water several times until the pH value was neutral. The washed powder was dried under vacuum at 80 °C for 12 h before being subjected to further studies and designated as PJ-AC.

Physical characterizations

The crystalline phase of the resultant material was studied by powder XRD (Rint 1000, Rigaku, Japan) using $Cu_{K\alpha}$ radiation. Raman studies were performed using a Lab Ram HR 800 Raman dispersive spectrometer (Horiba, Japan). BET surface area measurements were carried out by using a Micromeritics ASAP 2010 surface area analyzer. Morphological features of the samples were recorded by using a scanning electron microscope (FE-SEM, S4700, Hitachi, Japan). XPS was also performed using a Multilab 2000 (Thermo Scientific, UK) with monochromator and $Al_{K\alpha}$ radiation ($h\nu = 1486.6$ eV).

Electrochemical characterization

The positive electrode was formulated with PJ-AC (80%), ketzen black (10%), and teflonized acetylene black (10% of TAB-2) in ethanol. The slurry was pressed over a stainless-steel mesh (16 mm diameter, 200 mm^2 area) and dried at 160 °C for 4 h in vacuum oven. Negative electrode was made with NG, super-P, and polyvinylidene fluoride as binder by keeping the ratio (80:10:10) with *N*-methyl-2-pyrrolidone (NMP). Finally, the slurry was coated on Cu foil and dried at 80 °C for 12 h under vacuum. All the electrochemical measurements were performed in standard CR2032 coin-cell configuration. Pre-lithiation of the graphite electrode and the specific capacity of positive and negative electrodes were conducted in two-electrode configuration with metallic Li. For Li-HEC assembly, PJ-AC loading was adjusted with respect to graphite by maintaining 80:10:10 ratios upon the formulation of the electrodes. Both half-cell and Li-HEC assemblies were separated by a porous polypropylene (Celgard 3401, USA) film and filled with 1 M $LiPF_6$ in ethylene carbonate (EC)/di-methyl carbonate (DMC) (1:1 *v/v*, Soulbrain Co. Ltd, Korea) solution. CV and electrochemical impedance spec-

troscopy (EIS) studies were performed using an electrochemical work station (Bio-Logic (SP-150), France). Galvanostatic charge–discharge studies were performed at different current densities using a conventional battery tester (WBCS 3000, Won-A-Tech, Korea) under ambient conditions.

Acknowledgements

This work was supported by the Energy Efficiency & Resources Core Technology Program of the Korea Institute of Energy Technology Evaluation and Planning (KETEP), granted financial resource from the Ministry of Trade, Industry & Energy, Republic of Korea. (20152010103470)

Keywords: activated carbon · biomass · energy density · graphene · Li-ion capacitor

[1] M. S. Whittingham, *Proc. IEEE* **2012**, *100*, 1518.
[2] M. M. Thackeray, C. Wolverton, E. D. Isaacs, *Energy Environ. Sci.* **2012**, *5*, 7854.
[3] V. Aravindan, J. Gnanaraj, Y.-S. Lee, S. Madhavi, *Chem. Rev.* **2014**, *114*, 11619.
[4] G. G. Amatucci, F. Badway, A. Du Pasquier, T. Zheng, *J. Electrochem. Soc.* **2001**, *148*, A930.
[5] I. Plitz, A. DuPasquier, F. Badway, J. Gural, N. Pereira, A. Gmitter, G. G. Amatucci, *Appl. Phys. A* **2006**, *82*, 615.
[6] L. Ye, Q. Liang, Y. Lei, X. Yu, C. Han, W. Shen, Z.-H. Huang, F. Kang, Q.-H. Yang, *J. Power Sources* **2015**, *282*, 174.
[7] K. Naoi, S. Ishimoto, J.-I. Miyamoto, W. Naoi, *Energy Environ. Sci.* **2012**, *5*, 9363.
[8] V. Aravindan, N. Shubha, W. C. Ling, S. Madhavi, *J. Mater. Chem. A* **2013**, *1*, 6145.
[9] V. Aravindan, W. Chuiling, S. Madhavi, *J. Mater. Chem.* **2012**, *22*, 16026.
[10] V. Aravindan, M. V. Reddy, S. Madhavi, S. G. Mhaisalkar, G. V. Subba Rao, B. V. R. Chowdari, *J. Power Sources* **2011**, *196*, 8850.
[11] V. Aravindan, W. Chuiling, M. V. Reddy, G. V. S. Rao, B. V. R. Chowdari, S. Madhavi, *Phys. Chem. Chem. Phys.* **2012**, *14*, 5808.
[12] L. Cheng, H. Q. Li, Y. Y. Xia, *J. Solid State Electrochem.* **2006**, *10*, 405.
[13] R. Gokhale, V. Aravindan, P. Yadav, S. Jain, D. Phase, S. Madhavi, S. Ogale, *Carbon* **2014**, *80*, 462.
[14] M. D. Stoller, S. Murali, N. Quarles, Y. Zhu, J. R. Potts, X. Zhu, H.-W. Ha, R. S. Ruoff, *Phys. Chem. Chem. Phys.* **2012**, *14*, 3388.
[15] V. Aravindan, D. Mhamane, W. C. Ling, S. Ogale, S. Madhavi, *ChemSusChem* **2013**, *6*, 2240.
[16] J. Lee, W. Shin, S. Lim, B. Kim, J. Choi, *Mater. Reneweable Sustainable Energy* **2014**, *3*, 1.
[17] H. Kim, K.-Y. Park, J. Hong, K. Kang, *Sci. Rep.* **2014**, *4*, 5278.
[18] S. W. Lee, N. Yabuuchi, B. M. Gallant, S. Chen, B.-S. Kim, P. T. Hammond, Y. Shao-Horn, *Nat. Nanotechnol.* **2010**, *5*, 531.
[19] J. H. Lee, N. Park, B. G. Kim, D. S. Jung, K. Im, J. Hur, J. W. Choi, *ACS Nano* **2013**, *7*, 9366.
[20] A. Jain, V. Aravindan, S. Jayaraman, P. S. Kumar, R. Balasubramanian, S. Ramakrishna, S. Madhavi, M. Srinivasan, *Sci. Rep.* **2013**, *3*, 3002.
[21] P. Sennu, H.-J. Choi, S.-G. Baek, V. Aravindan, Y.-S. Lee, *Carbon* **2016**, *98*, 58.
[22] M.-S. Park, Y.-G. Lim, J.-H. Kim, Y.-J. Kim, J. Cho, J.-S. Kim, *Adv. Energy Mater.* **2011**, *1*, 1002.
[23] A. Jain, R. Balasubramanian, M. P. Srinivasan, *Chem. Eng. J.* **2016**, *283*, 789.
[24] J. Yan, Q. Wang, T. Wei, Z. Fan, *Adv. Energy Mater.* **2014**, *4*, 1300816.
[25] L. Wei, G. Yushin, *Nano Energy* **2012**, *1*, 552.
[26] K. Karthikeyan, S. Amaresh, S. N. Lee, X. Sun, V. Aravindan, Y.-G. Lee, Y. S. Lee, *ChemSusChem* **2014**, *7*, 1435.
[27] T. Aung, F. Koike, *J. Arid Environ.* **2015**, *120*, 87.
[28] A. J. Urfi, N. K. Tiwary, *Curr. Sci.* **2015**, *108*, 1973.
[29] A. C. Ferrari, J. Robertson, *Phys. Rev. B* **2000**, *61*, 14095.
[30] F. Tuinstra, J. L. Koenig, *J. Chem. Phys.* **1970**, *53*, 1126.
[31] J. Hodkiewicz, http://www.laboratoryequipment.com/articles/2011/06/characterizing-carbon-nanomaterials **2011**.
[32] B. Li, F. Dai, Q. Xiao, L. Yang, J. Shen, C. Zhang, M. Cai, *Energy Environ. Sci.* **2016**, *9*, 102.
[33] J. Baltrusaitis, C. R. Usher, V. H. Grassian, *Phys. Chem. Chem. Phys.* **2007**, *9*, 3011.
[34] Z. Yang, M. Xu, Y. Liu, F. He, F. Gao, Y. Su, H. Wei, Y. Zhang, *Nanoscale* **2014**, *6*, 1890.
[35] B. Kumar, M. Asadi, D. Pisasale, S. Sinha-Ray, B. A. Rosen, R. Haasch, J. Abiade, A. L. Yarin, A. Salehi-Khojin, *Nat. Commun.* **2013**, *4*, 2819.
[36] Q. Wang, L. Jiao, H. Du, Y. Si, Y. Wang, H. Yuan, *J. Mater. Chem.* **2012**, *22*, 21387.
[37] G. Wang, J. Zhang, S. Kuang, S. Liu, S. Zhuo, *J. Power Sources* **2014**, *269*, 473.
[38] N. Dwivedi, R. J. Yeo, N. Satyanarayana, S. Kundu, S. Tripathy, C. S. Bhatia, *Sci. Rep.* **2015**, *5*, 7772.
[39] T. P. Kumar, T. S. D. Kumari, A. M. Stephan, *J. Indian Inst. Sci.* **2009**, *89*, 393.
[40] T. Aida, K. Yamada, M. Morita, *Electrochem. Solid-State Lett.* **2006**, *9*, A534.
[41] S. Zhang, N. Pan, *Adv. Energy Mater.* **2015**, *5*, 1401401.
[42] J. J. Ren, L. W. Su, X. Qin, M. Yang, J. P. Wei, Z. Zhou, P. W. Shen, *J. Power Sources* **2014**, *264*, 108.
[43] J. H. Lee, W. H. Shin, M.-H. Ryou, J. K. Jin, J. Kim, J. W. Choi, *ChemSusChem* **2012**, *5*, 2328.
[44] M. Liu, L. Zhang, P. Han, X. Han, H. Du, X. Yue, Z. Zhang, H. Zhang, G. Cui, *Part. Part. Syst. Charact.* **2015**, *32*, 1006.
[45] W. J. Cao, J. P. Zheng, *J. Power Sources* **2012**, *213*, 180.
[46] T. Wang, L.-X. Wang, D.-L. Wu, W. Xia, D.-Z. Jia, *Sci. Rep.* **2015**, *5*, 9591.

Received: December 6, 2015
Published online on March 18, 2016